6

CFD-based Evaluation of Interfacial Flows

Kei Ito[1], Hiroyuki Ohshima[1], Takaaki Sakai[1] and Tomoaki Kunugi[2]
[1]*Japan Atomic Energy Agency*
[2]*Kyoto University*
Japan

1. Introduction

Gas-liquid two-phase flows with interfacial deformations have been studied in various scientific and industrial fields. However, owing to the complexity of interfacial transient behaviors, the full understanding of gas-liquid two-phase flows is extremely difficult. For example, the occurrence condition of gas entrainment (GE) from free surface is not yet clarified even though a number of studies have been conducted by a lot of researchers. Unexpected GE phenomena often cause problems with equipments or troubles in plant operations (e.g. pump failure) and suppression of their occurrences by flow optimization is strongly required from the viewpoints of operation rates and safety. Therefore, the high-level understanding of interfacial flows is very important and should be achieved appropriately based on mechanistic considerations.
In this Chapter, the authors propose two methodologies to evaluate the GE phenomena in fast reactors (FRs) as an example of interfacial flows. One is a CFD-based prediction methodology (Sakai et al., 2008) and the other is a high-precision numerical simulation of interfacial flows. In the CFD-based prediction methodology, a transient numerical simulation is performed on a relatively coarse computational mesh arrangement to evaluate flow patterns in FRs as the first step. Then, a theoretical flow model is applied to the CFD result to specify local vortical flows which may cause the GE phenomena. In this procedure, two GE-related parameters, i.e. the interfacial dent and downward velocity gradient, are utilized as the indicators of the occurrence of the GE phenomena. On the other hand, several numerical algorithms are developed to achieve the high-precision numerical simulation of interfacial flows. In the development, an unstructured mesh scheme is employed because the accurate geometrical modeling of the structural components in a gas-liquid two-phase flow is important to simulate complicated interfacial deformations in the flow. In addition, as an interface-tracking algorithm, a high-precision volume-of-fluid algorithm is newly developed on unstructured meshes. The formulations of momentum and pressure calculations are also discussed and improved to be physically appropriate at gas-liquid interfaces. These two methodologies are applied to the evaluation of the GE phenomena in experiments. As a result, it is confirmed that both methodologies can evaluate the occurrence conditions of the GE phenomena properly.

2. Brief description of GE phenomena

The GE phenomena can be observed in a lot of industrial plants with gas-liquid interfaces, e.g. pump sump. Therefore, the GE phenomena have been studied theoretically and

Source: Computational Fluid Dynamics, Book edited by: Hyoung Woo OH,
ISBN 978-953-7619-59-6, pp. 420, January 2010, INTECH, Croatia, downloaded from SCIYO.COM

experimentally in many years (Maier, 1998). In the experiments, the onset condition of the GE phenomena in a reservoir tank or main pipe with branch pipe was investigated in detail. As a result, the onset conditions of the GE phenomena are summarized as the function of Froude number (*Fr*) (Zuber, 1980):

$$\frac{H_{GE}}{d_b} = b_1 Fr^{b_2}, \tag{1}$$

where H_{GE} is the critical interfacial height of the GE phenomena, d_b is the diameter of a branch. b_1 and b_2 are the constants determined depending on the geometrical configurations in each experimental apparatus. Froude number is defined as

$$Fr = \frac{v_d}{\sqrt{\frac{\Delta\rho}{\rho_l} g d_b}}, \tag{2}$$

where v_d is the liquid velocity (suction velocity) in a branch, ρ_l is the liquid density, $\Delta\rho$ is the density difference between liquid and gas phases and g is the gravitational acceleration. Equation 1 can be derived from theoretical considerations with the Bernoulli equation (Craya, 1949), i.e. Eq. 1 implies the energy conservation law between potential and kinetic energies. Therefore, Eq. 1 is widely accepted among researchers of the GE phenomena.

The authors are interested in the GE phenomena at the gas-liquid interface in the primary circuit of FRs. It is well known that FR cycle technologies are expected to provide realistic solutions to global issues of energy resources and environmental conservations because they are efficient for not only the reduction of carbon dioxide emission but also the effective use of limited resources (Nagata, 2008). However, large-scale FRs have positive void reactivity, i.e. core power increases when gas bubbles flow into the core through the primary circuit. Moreover, gas bubbles in the primary circuit may cause the performance degradation of the heat exchangers. Therefore, the GE phenomena should be suppressed to reduce the number of the gas bubbles in the primary circuit and to achieve the stable operation (without power disturbances) of FRs. The GE phenomena in FRs are caused at the gas-liquid interface in an upper plenum region of the reactor vessel (the region located above the core). As showin in Fig. 1, the GE phenomena in FRs have been classified into three patterns, i.e. waterfall, interfacial disturbance and vortical flow types (Eguchi et al., 1984). Former two patterns can be suppressed by reducing the horizontal velocity at the gas-liquid interface. However, the GE phenomena caused by vortical flows is very difficult to determine a suppression criterion because the vortical flows at the gas-liquid interface are formed very locally and transiently. In fact, most vortical flows are initiated as the wake flows behind obstacles at the gas-liquid interface, e.g. inlet and/or outlet pipes in the upper plenum region, and intensified by interacting with local downward flows. Therefore, the suppression criterion of the GE phenomena caused by vortical flows should be determined based on local complicated flow patterns. In this case, a rather simple equation like Eq. (1) can not be applied to the evaluation of the GE phenomena and the property of vortical flows should be considered to the evaluation (Daggett & Keulegan, 1974). The authors propose two methodologies to evaluate the GE phenomena caused by vortical flows in FRs.

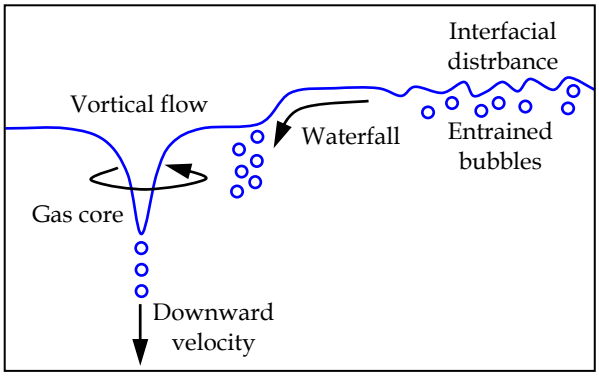

Fig. 1. GE phenomena in FRs

3. CFD-based prediction methodology

3.1 Basic concept

For the evaluation of the GE phenomena in FRs, complicated flows (vortical flows) which cause the GE phenomena have to be understood appropriately. However, it is highly difficult to predict the vortical flow patterns in complicated geometrical system configurations of FRs. In this case, CFD can be the efficient tool to evaluate the vortical flows in such a complicated FR system. Therefore, the authors propose a GE evaluation methodology in combination with CFD results (CFD-based prediction methodology) (Sakai et al., 2008). In the CFD-based prediction methodology, first, a transient numerical simulation of vortical flows is performed on a relatively coarse mesh to reduce the computational cost. For the same reason, interfacial deformations are not considered and the interfaces are modeled as the free-slip walls in the transient numerical simulation. Owing to these simplifications, the vortical flows can not be reproduced completely in the CFD result. Then, a theoretical flow model is applied to the CFD result to compensate for the mesh coarseness and to determine the strengths of each vortical flow. In the CFD-based prediction methodology, the Burgers theory (Burgers, 1948) is employed to calculate the gas core length (interfacial dent caused by the vortical flow) which is an important indicator to evaluate the GE phenomena.

3.2 Vortical flow model

In the CFD-based prediction methodology, the Burgers theory is employed as a vortical flow model. The Burgers theory is derived as a strict solution of the axisymmetric Navier-Stokes (N-S) equation:

$$u_r = -\frac{1}{2}\alpha r, \tag{3}$$

$$u_\theta = \frac{\Gamma_\infty}{2\pi r}\left[1-\exp\left\{-\left(\frac{r}{r_0}\right)^2\right\}\right], \tag{4}$$

$$u_z = \alpha\left(z - h_\infty\right), \tag{5}$$

where r, θ and z show the radial, tangential and axial directions, respectively (u_r, u_θ and u_z are the velocity components of each direction). α is the downward velocity gradient, r_0 is the specific radius of a vortical flow and h_∞ is the standard interfacial height at the far point from the vortical flow. Here, α and r_0 are related theoretically as

$$r_0 = 2\sqrt{\upsilon/\alpha}\,. \tag{6}$$

From the momentum balance equation in radial and axial directions, the equation of interfacial shape can be obtained as

$$g\frac{dh}{dr} = \frac{u_\theta^2}{r}, \tag{7}$$

where h is the interfacial height. Here, Eq. 7 is based on the assumption that the advection terms in the N-S equation is negligible compared to the pressure or gravitational term (Andersen et al., 2003). By substituting Eq. 4 into Eq. 7, the gas core length (the interfacial dent at the center of the vortical flow) is calculated as

$$L_{gc} = \frac{\log 2}{g}\left(\frac{\alpha\Gamma_\infty}{2\pi\upsilon}\right)^2, \tag{8}$$

where L_{gc} is the gas core length, Γ_∞ is the circulation (at the free vortical flow region) of a vortical flow and υ is the dynamic viscosity of liquid phase. In Eq. 8, α and Γ_∞ are necessary to calculate the gas core length. Therefore, in the CFD-based prediction methodology, these values are calculated by using the CFD result. As the first step of the calculation procedure, the second invariant of the velocity deformation tensor is calculated at the gas-liquid interface based on the CFD result to evaluate the strength of each vortical flow (Hunts et al., 1988). In this stage, vortical flows are extracted as the regions with negative second invariant, and the centers of each vortical flow are determined as the points with the minimum second invariant. For the strong vortical flows (with highly negative second invariant) which may causes the GE phenomena, the calculated second invariant is used again to determine the outer edges of each strong vortical flow. The initial outer edge is determined as the isoline of the second invariant with the value of zero. The reference circulation is calculated along the initial outer edge as

$$\Gamma_\infty = \int_C \vec{u}d\vec{s}, \tag{9}$$

where $\vec{u}$ is the velocity vector and the integral path C is determined as the outer edge ($d\vec{s}$ is the local tangential vector on C). Then, the outer edge is expanded radially, step by step, from the initial one to that twice larger than the initial one, and the circulation values are calculated on each expanded outer edge. Finally, to pick up the conservative value of the circulation, the maximum value is selected as the circulation of the vortical flow. On the other hand, the downward velocity gradient is calculated on the initial outer edge (isoline of the second invariant with the value of zero) as

$$\alpha = \frac{\int_C \vec{u}\cdot\vec{n}_C ds}{A}, \tag{10}$$

where $\vec{n}_C$ is the unit vector normal to the outer edge (*C*) and *A* is the area of the inner region (surrounded by the outer edge). *ds* is the local length of the outer edge. Eq. 10 shows the averaged downward velocity gradient in the inner region which is calculated as the averaged horizontal inlet flow rate into the inner region. By substituting these two calculated parameters into Eq. 7, the gas core length can be calculated based on the Burgers theory.

3.3 Two types of GE phenomena

In the FRs, the generation of the vortical flow with strong downward velocity is the key of the occurrence of the GE phenomena. Therefore, this flow pattern is modeled in two simple experiments to investigate types of the GE phenomena. Those simple experiments are performed by utilizing a cylindrical vessel which has an outlet pipe installed on the center of the bottom of the vessel. As for the working fluids, water and air at room temperature are employed in those simple experiments.

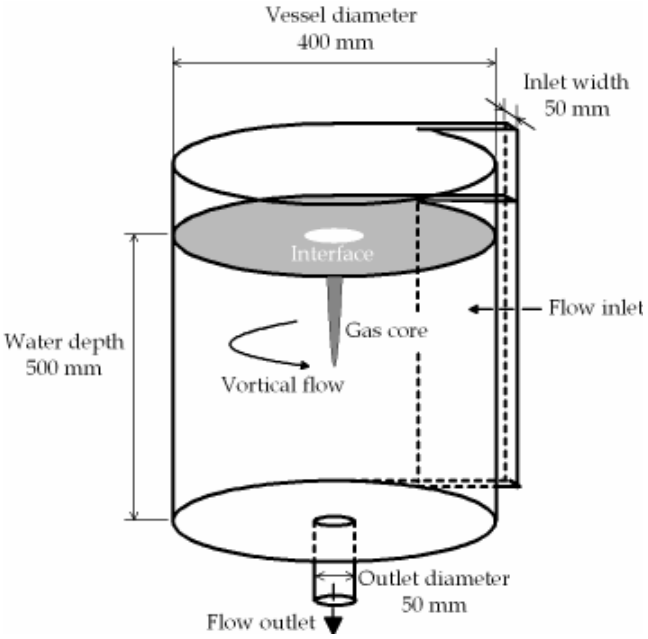

Fig. 2. Schematic view of Moriya's experimental apparatus

The first experiment was performed by Moriya (Moriya, 1998). As shown in Fig. 2, the inner diameter of the cylindrical vessel and outlet pipe are 400 and 50 mm, respectively. The water depth is kept at 500 mm. The water is driven by a pump and flowed into the cylindrical vessel in tangential direction through a rectangular inlet with the width of 40 mm. In the cylindrical vessel, a vortical flow is caused by this inlet flow and intensified by the downward flow towards the outlet pipe on the bottom of the vessel. Therefore, the strength of the vortical flow increases and the gas core became longer as the inlet flow rate increases. Finally, the GE phenomena occur when the tip of the gas core reached the outlet pipe. Then, a ring-plate whose inner and outer diameters were 100 and 400 mm was set on the gas-liquid interface to investigate the change in the GE phenomena. As a result, it was found

that the ring-plate made the downward velocity gradient near the gas core higher and caused bubble pinch-off from the tip of the gas core.
The second experiment was performed by Monji (Monji et al., 2004). For this experiment, a cylindrical vessel similar to the Moriya's (without a ring-plate) is employed. The inner diameter of the cylindrical vessel and outlet pipe are 200 and 12.5 mm, respectively. The water depth is kept at 250 mm and the width of the rectangular inlet is 20 mm. A vortical flow and gas core are generated in the cylindrical vessel with the same mechanism as the Moriya's experiment. In this (Monji's) experiment, typical bubble pinch-off from the tip of gas core was observed as shown in Fig.3 by utilizing a micro-scope. This bubble pinch-off occurred continuously from the gas core. In this case, the gas core length was only about 60 mm and the tip of the gas core had the diameter of approximately 0.5 mm.

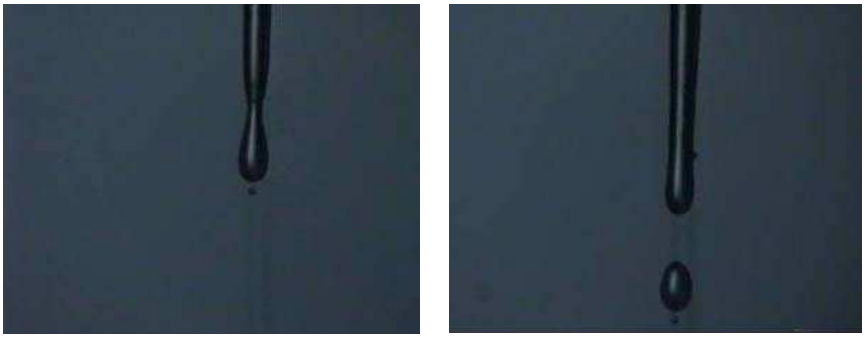

Fig. 3. Bubble pinch-off type of GE phenomena

From the results of these two experiments, the authors define the two types of the GE phenomena, i.e. a) elongated gas core type and b) bubble pinch-off type. It is evident that the elongated gas core type is caused by a strong vortical flow which makes the gas core length longer than a liquid depth. In addition, the experimental results show that the strong downward velocity gradient near the tip of a gas core can cause the bubble pinch-off. Therefore, in the CFD-based prediction methodology, the gas core length and downward velocity gradient should be considered as the indicators to evaluate two types of the GE phenomena.

3.4 Onset conditions of GE phenomena

In the CFD-based prediction methodology, the gas core length and downward velocity gradient are evaluated by Eqs. 8 and 10, respectively. However, it is necessary to determine the criteria of the GE occurrences for the prediction of the GE phenomena. In this section, the criteria are determined based on the CFD results of the simple experiments (like the Moriya's or Monji's experiment).
In this study, the CFD of the Monji's, Moriya's and Sakai's (Sakai et al., 1997) experiments are performed under the boundary conditions consistent with the experimental conditions. For the CFD of those experiments, the authors utilize the FLUENT code. In the CFD, the 2nd order up-wind scheme is applied for the advection term of the N-S equation, and the turbulent model is not employed to diminish the model dependency to the CFD result. In addition, the interfacial deformation model is not employed to reduce the computational cost, and the gas-liquid interface is treated as a flat free-slip wall. Figure 4 shows the computational mesh for the CFD of the Monji's experiment, which is subdivided by only

hexahedral cells. As for boundary conditions, the uniform velocity condition is applied to the inlet, and the constant pressure condition is applied to the outlet. The transient CFD is performed for over 100 seconds to obtain the quasi-steady result.

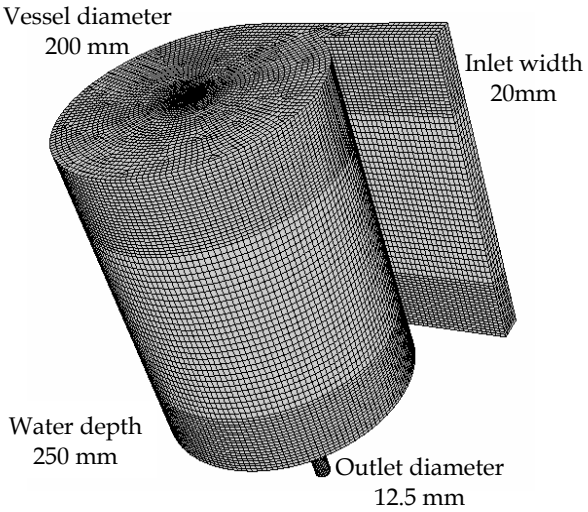

Fig. 4. Computational mesh for CFD of Monji's experiment

Figure 5 shows the comparison of the circumferential velocity distributions in the experimental and CFD results. It is evident that the CFD result agrees well with the experimental result in the free vortical flow regions, and therefore, the circulation can be evaluated accurately by Eq. 9 in the CFD-based prediction methodology. The CFD of the Moriya's experiments is also performed and the downward velocity distribution in the CFD result is compared to the experimental result. As shown in Fig. 6, the CFD can not reproduce the experimental result near the center of the vortical flow. However, the CFD results approach to the experimental results as the radius from the center of the vortical flow

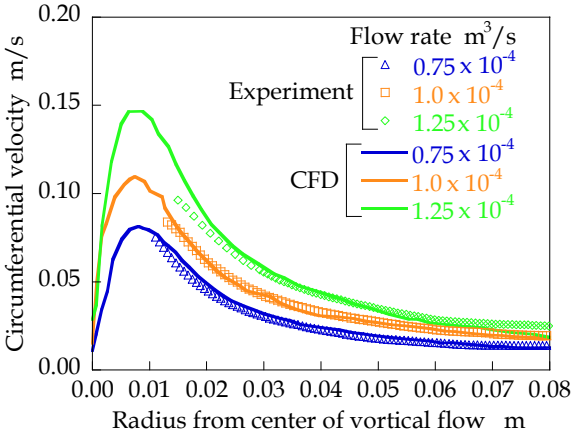

Fig. 5. Cicumferential velocity in CFD result of Moji's experiment

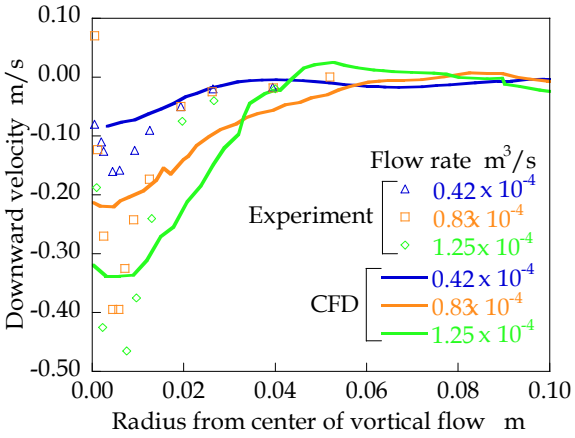

Fig. 6. Downward velocity in CFD result of Moriya's experiment

increases and the downward velocities converge to zero. This behavior shows that the areas of the regions with non-zero downward velocity are the almost same in the CFD and experimental results near the center of the vortical flow. Therefore, the averaged downward velocity can be evaluated accurately by Eq. 10 in the CFD-based prediction methodology.
Figure 7 shows the gas core length evaluated by the CFD-based prediction methodology. In this figure, two non-dimensional numbers are introduced to organize the CFD results, which are defined as

$$\alpha^* = \frac{\alpha \upsilon}{g h_\infty}, \tag{11}$$

$$\Gamma^* = \frac{\Gamma_\infty}{\upsilon}, \tag{12}$$

In reference to Eq. 8, the ratio of the gas core length to the liquid depth (non-dimensional gas core length) can be written as

$$\frac{L_{gc}}{h_\infty} = K \cdot \alpha^* \cdot \Gamma_\infty^{*2}, \tag{13}$$

where K is 4.389 × 10^{-3}. Therefore, the lateral axis of Fig. 7 is proportional to the non-dimensional gas core length evaluated by the CFD-based prediction methodology, and the vertical axis shows the non-dimensional gas core length in the experimental results (the subscripts EXP and CFD show the experimental result and the values evaluated based on the CFD result, respectively). From these definitions, it is apparent that the elongated gas core type GE phenomena occur when the non-dimensional gas core length excesses unity. Therefore, the indicator of the elongated gas core type of the GE phenomena should be determined based on Eq. 13 if the CFD-based prediction methodology can evaluate the non-dimensional gas core length exactly. In that case, the plots have to lie on the line of the Burgers theory (the red bold line in Fig. 7). Actually, the plots are scattered almost within the range from one-third to three-times of the Burgers theory (the error bars of the lateral

values show the transient fluctuation in CFD results). Therefore, the authors determine the first onset condition for the elongated gas core type of the GE phenomena as

$$\alpha^*_{CFD}\left(\Gamma^*_\infty\right)^2_{CFD} < 76. \tag{14}$$

Equation 14 is derived from Eq. 13 with the consideration of the three times allowance, and is shown by the red left dotted line in Fig. 6. By employing this criterion, the occurrences of the elongated gas core type of the GE phenomena can be predicted with appropriate conservativeness.

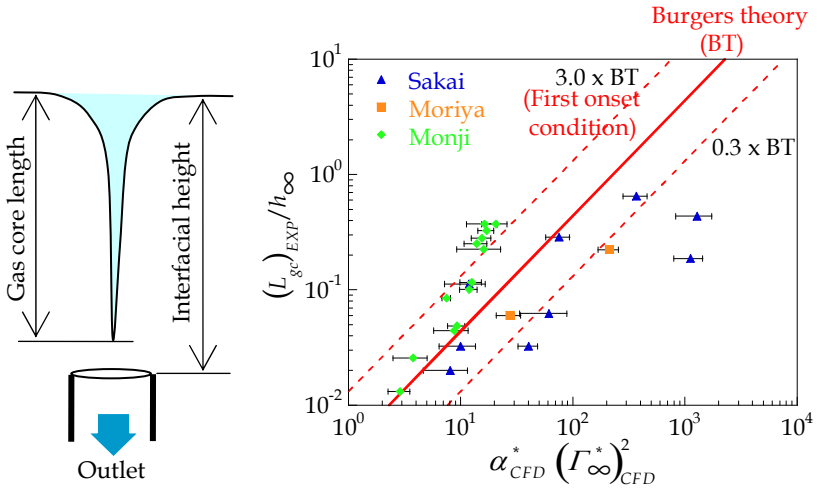

Fig. 7. Prediction accuracy of gas core length

Figure 8 shows the downward velocity gradient evaluated by the CFD-based prediction methodology. As mentioned in Section 3.3, it is apparent that the bubble pinch-off type of

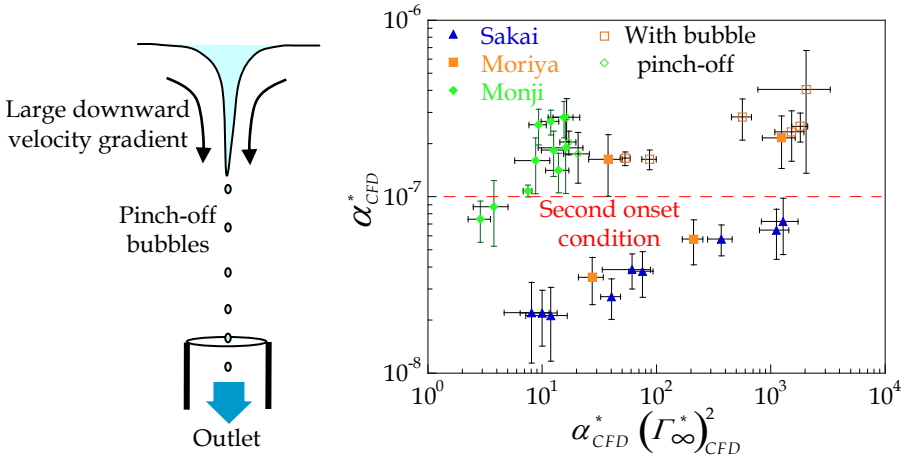

Fig. 8. Bubble pinch-off behavior

the GE phenomena (open plots) occurs when the downward velocity gradient becomes large. Therefore, the authors determine the second onset condition for the bubble pinch-off type of the GE phenomena empirically as

$$\alpha^*_{CFD} < 10^{-7}. \tag{15}$$

The occurrence of the GE phenomena in FRs is predicted by using these two conditions (Eqs. 14 and 15).

3.5 Application to GE phenomena in FRs

For the validation of the CFD-based prediction methodology, the GE phenomena in a 1/1.8 scale partial model (Kimura et al., 2008) are evaluated. Figure 9 shows the 1/1.8 scale partial model in which the geometrical configurations of the FR system components, e.g. the pipes, are reproduced accurately. The dipped plate (horizontal plate) is also reproduced in the model to reduce the horizontal velocity at the interface for the prevention of the waterfall and interfacial disturbance. In this model, the inlet horizontal flow generate wake flows (vortical flows) behind the pipes and the vortical flows are intensified by interacting with the suction flow around the pipes toward the gaps between the pipes and dipped plate. The experiments were performed under several conditions for inlet and suction velocities and/or liquid depth.

In this study, the evaluation of the GE phenomena by the CFD-based prediction methodology is performed in terms of the rated and GE conditions. Under the rated condition, the inlet and suction velocities are set to be the rated condition in FRs, and the liquid depth is also determined from the rated condition in FRs. In the experiment under the rated condition, no strong vortical flow was observed, and therefore, no GE phenomenon was observed. On the other hand, under the GE condition, the inlet and suction velocities are enhanced to five times rated condition, and the liquid depth is reduced to about half of the rated condition. Owing to this very severe condition setting, the GE phenomena were observed in the experiment under the GE condition.

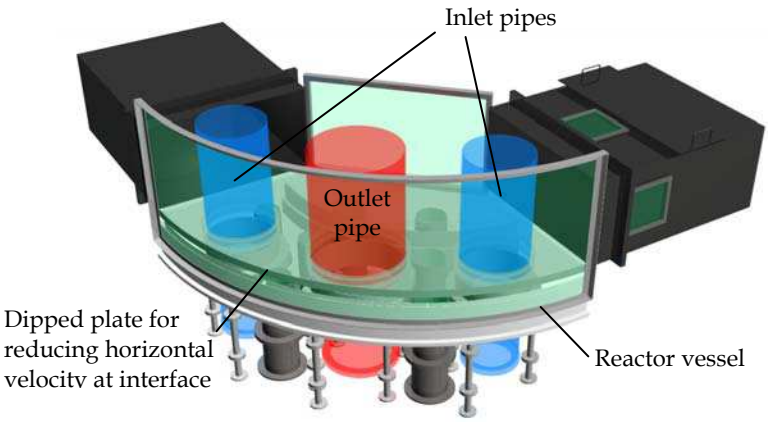

Fig. 9. 1/1.8 scale partial model

The CFD of the 1/1.8 scale partial model is performed by utilizing the FLUENT code. To simulate the complicated flow pattern in the 1/1.8 scale partial model, the RNG

(renormalization group) k-ε turbulent model is employed in the CFD. It should be mentioned that relatively coarse computational mesh (cell size is about twenty or thirty millimeters) is employed to reduce the computational cost.
Figure 10 shows the evaluation results of the GE phenomena under the two conditions (Uchibori et al., 2006). In the figures, the vertical dotted line shows the indicator of the elongated gas core type of the GE phenomena (Eq. 14) and the horizontal one is the indicator of the bubble pinch-off type of the GE phenomena (Eq. 15). It is evident that no GE phenomenon is evaluated under the rated condition, and the occurrence of the GE phenomena is predicted under the GE condition. This tendency agrees with the experimental results, and therefore, it is confirmed that the CFD-based prediction methodology can evaluate the GE phenomena in FRs accurately.

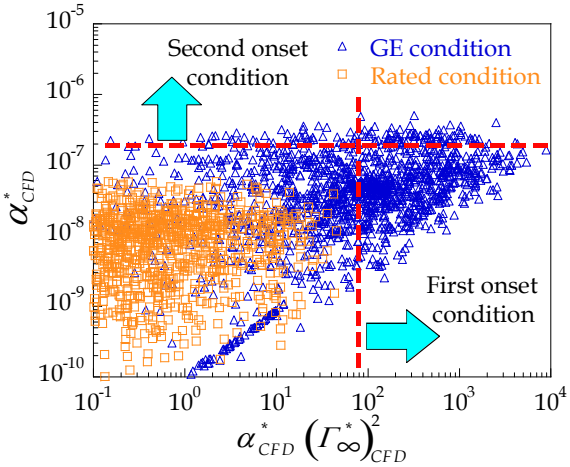

Fig. 10. Assessment of GE occurrence by CFD-based prediction methodology

3.6 Improvement of CFD-based prediction methodology

The CFD-based prediction methodology is very effective for the evaluation of the GE phenomena in FRs. However, some physical mechanisms are neglected in the CFD-based prediction methodology for the simplification. For example, the surface tension is not included in Eq. 7, and therefore, gas core lengths can be overestimated by Eq. 8. Recently, the authors have developed the improved CFD-based prediction methodology by introducing the surface tension (Ito et al., 2008). In this improved methodology, the mechanical balance equation between the centrifugal, gravitational and surface tension forces (Andersen et al. 2003) is employed instead of Eq. 7. The mechanical balance equation is written as

$$g\frac{dh}{dr}=\frac{u_\theta^2}{r}-\frac{\sigma}{\rho}\frac{d\kappa}{dr}, \tag{16}$$

where s is the surface tension coefficient. The interfacial curvature κ is calculated as

$$\kappa=\frac{h'}{r\left\{1+\left(h'\right)^2\right\}^{1/2}}+\frac{h''}{\left\{1+\left(h'\right)^2\right\}^{3/2}}, \tag{17}$$

where $h' = dh/dr$, $h'' = d^2h/dr^2$. Then, the gas core length with the consideration of the surface tension is calculated as

$$L_{gc} = \frac{\log 2}{g}\left(\frac{\Gamma_\infty}{2\pi r_0}\right)^2 - \frac{4\sigma W}{\rho g r_0}. \tag{18}$$

where W is the function of the Froude and Weber numbers. The improved CFD-based prediction methodology has been applied to the GE phenomena in the Monji's simple experiment conducted under the several fluid temperatures or surfactant coefficient concentrations. As a result, the effect of the fluid property (the dynamic viscosity and/or surface tension coefficient) was evaluated accurately by the improved CFD-based prediction methodology.

4. High-precision numerical simulation of interfacial flow

4.1 General description of high-precision numerical simulation algorithm

In order to reproduce the GE phenomena, the authors have developed high-precision numerical simulation algorithms for gas-liquid two-phase flows. In the development, two key issues are addressed for the simulation of the GE phenomena in FRs. One is the accurate geometrical modeling of the structural components in the gas-liquid two-phase flow, which is important to simulate accurately vortical flows generated near the structural components. This issue is addressed by employing an unstructured mesh. The other issues is the accurate simulation of interfacial dynamics (interfacial deformation), which is addressed by developing an interface-tracking algorithm based on the high-precision volume-of-fluid algorithm on unstructured meshes (Ito et al., 2007). The physically appropriate formulations of momentum and pressure calculations near a gas-liquid interface are also derived to consider the physical mechanisms correctly in numerical simulations (Ito & Kunugi, 2009).

4.2 Development of high-precision volume-of-fluid algorithm on unstructured meshes

In this study, a high-precision volume-of-fluid algorithm, i.e. the PLIC (Piecewise Linear Interface Calculation) algorithm (Youngs, 1982) is chosen as the interface-tracking algorithm owing to its high accuracy on numerical simulations of interfacial dynamics. In the volume-of-fluid algorithm, the following transport equation is solved to track interfacial dynamic behaviors:

$$\frac{\partial f}{\partial t} + \vec{u} \cdot \nabla f = 0, \tag{19}$$

where f is the volume fraction of the interested fluid in a cell with the range from zero to unity, i.e. f is unity if a cell is filled with liquid; f is zero if a cell is filled with gas; f is between zero and unity if an interface is located in a cell. To enhance the simulation accuracy, the PLIC algorithm is employed to calculate Eq. 19. In the procedures of the PLIC algorithm, the calculation of the volume fraction by Eq. 19 is as follows:

1. an unit vector normal to the interface ($\vec{n}$) in an interfacial cell is calculated based on the volume fraction distribution at time level n (f^n);
2. a segment of the interface is reconstructed as a piecewise linear line;

3. volume fraction transports through cell-faces on the interfacial cell are calculated based on the location of the reconstructed interface;
4. the volume fraction distribution at time level $n + 1$ (f^{n+1}) is determined.

The PLIC algorithm and its modifications (e.g. Harvie & Fletcher, 2000; Kunugi, 2001; Renardy & Renardy, 2002; Pilliod & Puckett, 2004) have been applied to a lot of numerical simulations of various multi-phase flows.

Then, to address the requirement for the accurate geometrical modeling of complicated spatial configurations, an unstructured mesh scheme was employed, so that the authors improve the PLIC algorithm originally developed on structured meshes to be available even on unstructured meshes. In concrete terms, the algorithms for the calculation of the unit vector normal to an interface, reconstruction of an interface, calculation of volume fraction transports through cell-faces and surface tension model are newly developed with high accuracies on unstructured meshes. Usually, the unit vector normal to an interface ($\vec{n}$) is calculated based on the derivatives of a given volume fraction distribution. In this study, the Gauss-Green theorem (Kim et al., 2003) is utilized to achieve the derivative calculation on unstructured meshes. Therefore, the non-unit vector is calculated in an interfacial cell as

$$\vec{n} = \frac{1}{V_c}\int_{\Sigma} f_f d\vec{A} = \frac{1}{V_c}\sum_{f} f_f \vec{A}_f \tag{20}$$

where V_c is the cell volume and $\vec{A}$ is the area vector normal to a cell-face, which shows the area of the cell-face by its norm. Subscripts f shows the cell-face value, and f_f is interpolated from the given cell values. The summation in Eq. 20 is operated on all cell-faces on a cell. The unit vector is obtained by subdividing the calculated vector by the norm of the vector. It is confirmed that this calculation algorithm is robust and accurate even on unstructured meshes. In the interface reconstruction algorithm, a gas-liquid interface is reconstructed as a piecewise linear line in an interfacial cell, which is normal to the unit vector ($\vec{n}$) and is located so that the partial volume of the interfacial cell determined by the reconstructed interface coincides with the liquid (or gas) volume in the cell. In general, this reconstruction procedure is accomplished by the Newton-Raphson algorithm, i.e. an iterative algorithm (Rider & Kothe, 1998). However, a direct calculation algorithm, i.e. a non-iterative algorithm, in which a cubic equation is solved to determine the location of the reconstructed interface, has been developed on a structured mesh, and it is reported that the direct calculation algorithm provides more accurate solutions with the reduced computational cost (Scardvelli & Zaleski, 2000). Furthermore, the direct calculation algorithm was extended to two-dimensional unstructured meshes and succeeded in reducing the computational costs also on unstructured meshes (Yang & James, 2006). In this study, the authors newly develop the direct calculation algorithm on three-dimensional unstructured meshes. In addition, to achieve more accurate calculation of an interfacial curvature compared to the conventional calculation algorithm, i.e. the CSF (Continuum Surface Force) algorithm (Brackbill, 1992), the RDF (Reconstructed Distance Function) algorithm (Cummins et al., 2005) is extended to unstructured cells. To establish the volume conservation property violated by the excess or too little transport of the volume fraction, the volume conservative algorithm is developed by introducing the physics-basis correction algorithm.

As the verifications of the developed PLIC algorithm on unstructured meshes, the slotted-disk revolution problem (Zalesak, 1979) is solved on structured and unstructured meshes. The simulation results of the slotted-disk revolution problem by various volume-of-fluid

algorithms are well summarized by Rudman (Rudman, 1997). Therefore, the numerical simulations are performed under the same simulation conditions as Rudman's. Figure 11 shows the simulation conditions. In a 4.0 x 4.0 simulation domain, a slotted-disk with the radius of 0.5 and the vertical slot width of 0.12 is located. Initially, the volume fraction is set to be unity in the slotted-disk and zero outside the slotted-disk. Then, the slotted-disk is revolved around the domain center (2.0, 2.0) in counterclockwise direction. After one revolution, the volume function distribution is compared to the initial distribution to evaluate the numerical error.

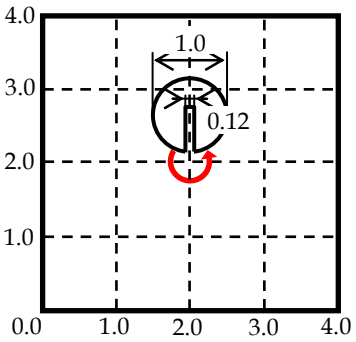

Fig. 11. Rudman's simulation conditions of slotted-disk revolution problem

Table 1 shows the simulation results. The structured mesh consists of 40,000 uniform square cells with the size of 2.0 x 2.0, and the unstructured mesh consists of about 40,000 irregular (triangular) cells. Upper four simulation results on the table are obtained by Rudman. On the structured mesh, it is evident that the developed PLIC algorithm shows much better simulation accuracy than the conventional volume-of-fluid algorithms, i.e. the SLIC (Simple Line Interface Calculation) algorithm (Noh & Woodward, 1976), the SOLA-VOF algorithm (Hirt & Nichols, 1981) and the FCT-VOF algorithm (Rudman, 1997). Moreover, the developed PLIC algorithm provides slightly more accurate simulation result than the original PLIC algorithm (Youngs, 1982). Therefore, the developed PLIC algorithm is confirmed to have the capability to simulate interfacial dynamic behaviors accurately. On the unstructured mesh, the simulation accuracy of the developed PLIC algorithm is much higher than that of the CICSAM (Compressive Interface Capturing Scheme for Arbitrary Meshes) (Ubbink & Issa, 1999) algorithm. However, the numerical error on the unstructured mesh is about 1.4 times larger than that on the structured mesh because the volume conservation property is highly violated by the excess or too little transport from the distorted cells on the unstructured mesh. Therefore, the numerical error is reduced to only 1.15 times larger than that on the structured mesh by employing the volume conservative algorithm. It should be mentioned that the volume conservative algorithm is efficient also for stabilizing the numerical simulations with large time increments (as shown in Fig. 12).

4.3 Physically appropriate formulations

To simulate interfacial dynamics accurately, it is necessary to employ not only the high-precision interface-tracking algorithm but also the physically appropriate formulations of the two-phase flow near a gas-liquid interface. Therefore, physics-basis considerations are conducted for the mechanical balance at a gas-liquid interface. In this study, the authors

Algorithm	Computational mesh	Numerical error
SLIC	Structured	8.38 x 10^{-2}
SOLA-VOF		9.62 x 10^{-2}
FCT-VOF		3.29 x 10^{-2}
PLIC		1.09 x 10^{-2}
Present		1.07 x 10^{-2}
Present	Unstructured	2.02 x 10^{-2}
CICSAM		1.50 x 10^{-2}
Present (volume conservative)		1.23 x 10^{-2}

Table 1. Numerical error in slotted-disk revolution problem

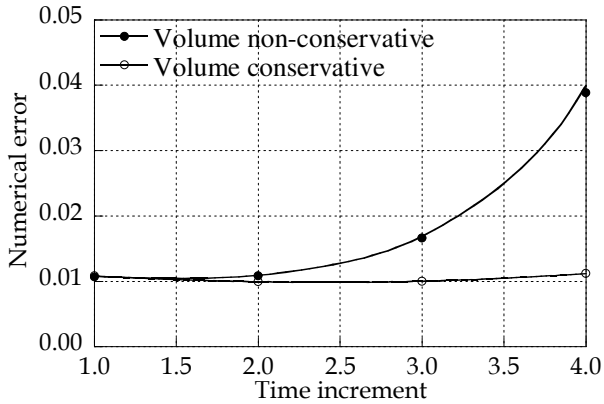

Fig. 12. Comparison of volume conservative and non-conservative algorithms

improve the formulations of momentum transport and pressure gradient at a gas-liquid interface.

In usual numerical simulations, the velocity at an interfacial cell is defined as a mass-weighted average of the gas and liquid velocities:

$$\vec{u} = \frac{\vec{u}_g \rho_g (1-f) V_c + \vec{u}_l \rho_l f V_c}{\rho V_c} = \frac{\vec{m}}{\rho} \tag{21}$$

where $\vec{u}$ and $\vec{m}$ the velocity and momentum vectors, respectively. The subscripts g and l shows the gas and liquid phases. This formulation is valid when the ratio of the liquid density to the gas density is small. However, in the numerical simulations of actual gas-liquid two-phase flows, the density ratio becomes about 1,000, and the liquid velocity dominates the velocity at an interfacial cell owing to the large density even when the volume fraction is small. Therefore, a physically appropriate formulation is derived to simulate momentum transport mechanism accurately. In the physically appropriate formulation, the velocity and momentum are defined independently

$$\vec{u} = (1-f)\vec{u}_g + f\vec{u}_l, \tag{22}$$

$$\vec{m} = (1-f)\rho_g \vec{u}_g + f\rho_l \vec{u}_l. \tag{23}$$

It is apparent that the velocity calculated by Eq. 22 is density-free and the volume-weighted average of the gas and liquid velocities. To validate the physically appropriate formulation, a rising gas bubble in liquid is simulated. As a result, the unphysical pressure distribution around the gas bubble caused by the usual formulation is eliminated successfully by the improved formulation (as shown in Fig. 13).

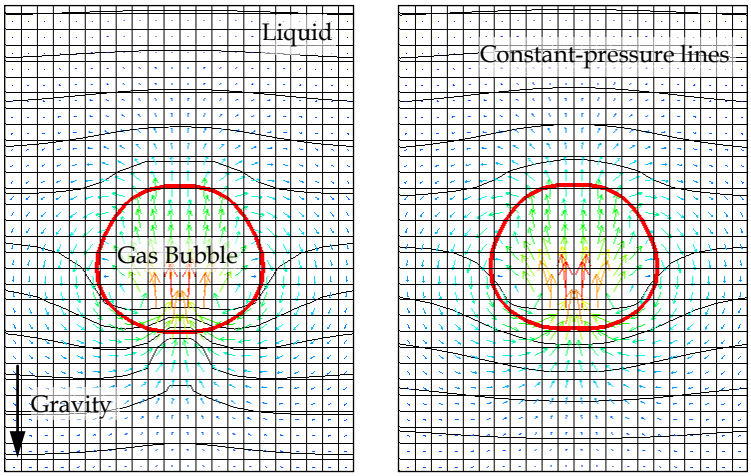

Fig. 13. Pressure distributions near interface of rising gas bubble: (a) Unphysical distribution caused by conventional algorithm, (b) Physically appropriate distribution with improved formulation

The other improvement is necessary to satisfy the mechanically appropriate balance between pressure and surface tension at a gas-liquid interface. In usual numerical simulations, the pressure gradient at an interfacial cell is defined as

$$\nabla p = \sum_{adjacent} \beta p, \tag{24}$$

where p is the pressure. The summation is performed on all adjacent cells to an interfacial cell, and β is the weighting factor for each adjacent cell. Equation 24 shows that the pressure gradient at an interfacial cell is calculated from the pressure distribution around the interfacial cell. However, the surface tension is calculated locally at an interfacial cell, and therefore, the balance between pressure and surface tension at the interfacial cell is not satisfied. The authors improved the formulation of the pressure gradient at an interfacial cell (Eq. 24) to be physically appropriate formulation which is consistent with the calculation of the surface tension at the interfacial cell. In the physically appropriate formulation, the pressure gradient at an interfacial cell is calculated as

$$p_f = p + (\nabla p)^t \cdot \frac{\vec{r}_f}{2}, \tag{25}$$

$$\frac{F-(\nabla p)^t}{\rho}=\frac{\sum_{sides}\gamma F-(\nabla p)_f}{\rho_f}, \tag{26}$$

$$\nabla p=\frac{\sum_f \vec{A}_f p_f}{V_c}, \tag{27}$$

where F is the surface tension and $(\nabla p)^t$ is the temporal pressure gradient for the calculation of p_f. $\vec{r}_f$ is the vector joining the cell-center of an interfacial cell to the cell-face-center on the interfacial cell. The summation in Eq. 26 is the interpolation from the cells on both sides of a cell-face to the cell-face, and γ is the weighting factor. The left side hand of Eq. 26 shows that the mechanical balance between pressure gradient and surface tension at an interfacial cell, and the right hand side shows the balance on a cell-face. In other words, the temporal pressure gradient at an interfacial cell becomes the same as the surface tension at the interfacial cell when the mechanical balance between pressure gradient and surface tension is satisfied on all cell-faces on the interfacial cell. Moreover, the mechanical balance on cell-faces can be satisfied easily because both the pressure gradient and surface tension are calculated locally on cell-faces. Therefore, above equations eliminate almost the numerical error in the usual calculation of the pressure gradient at an interfacial cell. To validate the improved formulation, a rising gas bubble in liquid is simulated again. Figure 14 shows the simulation result of velocity distribution around the bubble. The discontinuous velocity distribution caused by the usual formulation is eliminated completely by the improved formulation.

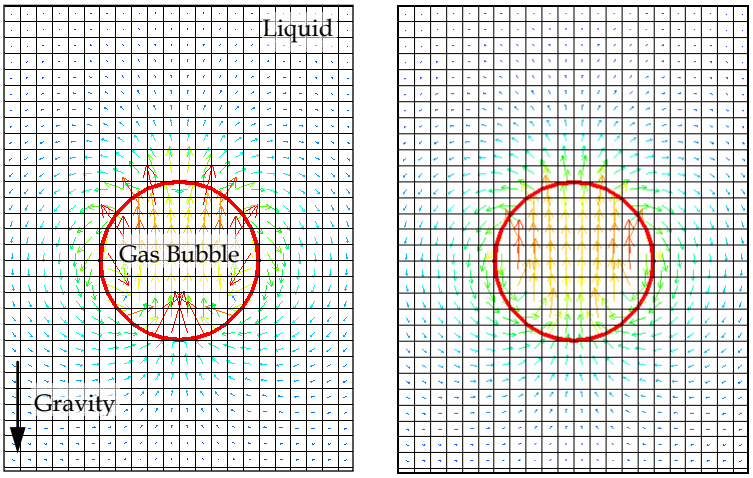

Fig. 14. Velocity distributions near interface of rising gas bubble: (a) Unphysical distribution caused by conventional algorithm, (b) Physically appropriate distribution with improved formulation

4.4 Numerical simulation of GE phenomena

The developed high-precision numerical simulation algorithms are validated by simulating the GE phenomena in a simple experiment (Ito et al. 2009). Figure 15 shows the

experimental apparatus (Okamoto et al., 2004) which is a rectangular channel with the width of 0.20 m in which a square rod with the edge length of 50 mm and square suction pipe with the inner edge length of 10 mm are installed. The liquid depth in the rectangular channel is 0.15 m. Working fluids are water and air at room temperature.

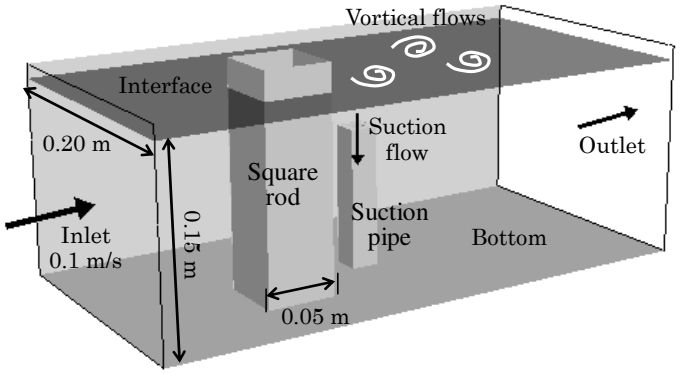

Fig. 15. Schematic view of Okamoto's experimental apparatus

In the rectangular channel, uniform inlet flow (0.10 m/s) from the left boundary (in Fig. 15) generates a wake flow behind the square rod when the inlet flow goes through the square rod. In the wake flow, a vortical flow is generated and advected downstream. Then, when the vortical flow passes across the region near the suction pipe, the vortical flow interacts with the suction (downward) flow (4.0 m/s in the suction pipe), and the vortical flow is intensified rapidly. Furthermore, a gas core is generated on the gas-liquid interface accompanied by this intensification of the vortical flow. Finally, when the gas core is elongated enough along the core of the vortical flow, the GE phenomena occur, i.e. the gas is entrained into the suction pipe.

In the numerical simulation, first, a computational mesh is generated carefully to simulate the GE phenomena accurately. Figure 16 shows the computational mesh. In this computational mesh, fine cells with the horizontal size of about 1.0 mm are applied to the region near the suction pipe in which the GE phenomena occur. In addition, to simulate the transient behavior of a vortical flow accurately, unstructured hexahedral cells with the horizontal size of about 3.0 mm are also applied to the regions around the square rod and that between the square rod and the suction pipe. Furthermore, the vertical size of cells is refined near the gas-liquid interface to reproduce interfacial dynamic behaviors. As for boundary conditions, uniform velocity conditions are applied to the inlet and suction boundaries. On the outlet boundary, hydrostatic pressure distribution is employed. The simulation algorithms employed in this chapter is summarized in Table 2.

In the numerical simulation, the development of the vortical flow and the elongation of the gas core are investigated carefully. As a result, the vortical flow develops upward from the suction mouth to the gas-liquid interface by interacting with the strong downward flow near the suction mouth. Then, the rapid gas core elongation along the center of the developed vortical flow starts when the high vortical velocity reached the gas-liquid interface. Finally, the gas core reaches the suction mouth and the GE phenomena (entrainment of the gas bubbles into the suction pipe) occur (as shown in Fig. 17). After a

General discritization scheme	Finite volume algorithm (Collocated variable arrangement)	
Velocity-pressure coupling	SMAC	
Discritization schemes for each term in the N-S equation	Unsteady term	1st order Euler
	Advection term	2nd order upwind
	Diffusion term	2nd order central
Interface tracking scheme	PLIC	
Momentum transport	Eqs. 22 and 23	
Pressure gradient	Eqs. 25, 26 and 27	

Table 2. General description of high-precision numerical simulation algorithms

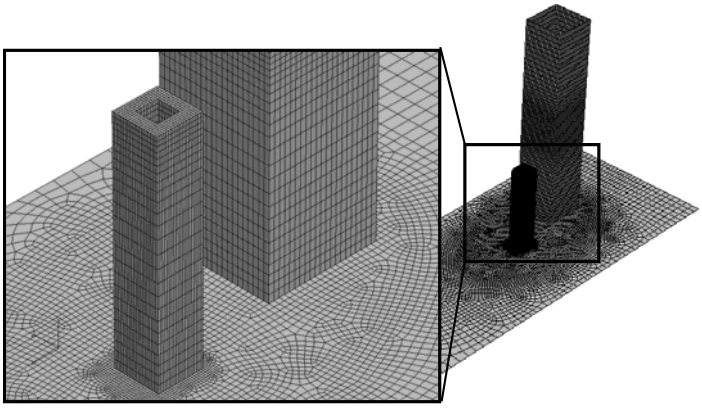

Fig. 16. Simulation mesh of Okamoto's experimental apparatus

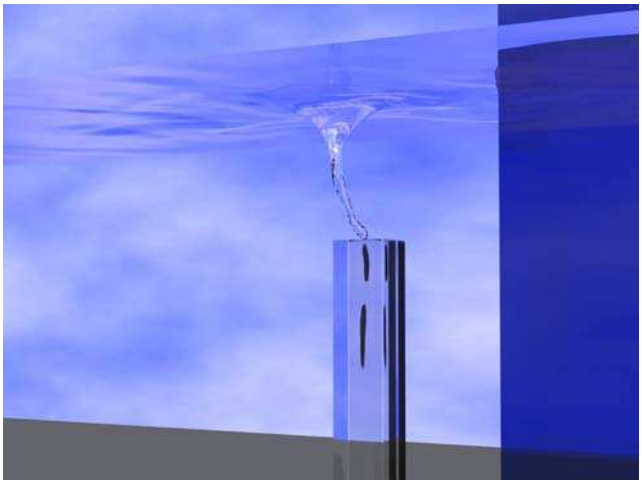

Fig. 17. Photorealistic visualization of GE phenomena

short period of the GE phenomena, the vortical flow is advected downstream, and the gas core length decreases rapidly. In this stage, the bubble pinch-off from the tip of the attenuating gas core is observed.

This GE phenomena observed in the simulation result is compared to the experimental result. In Fig. 18, it is evident that the very thin gas core provided in the experimental result is reproduced in the simulation result. In addition, as for the elongation of the gas core, the

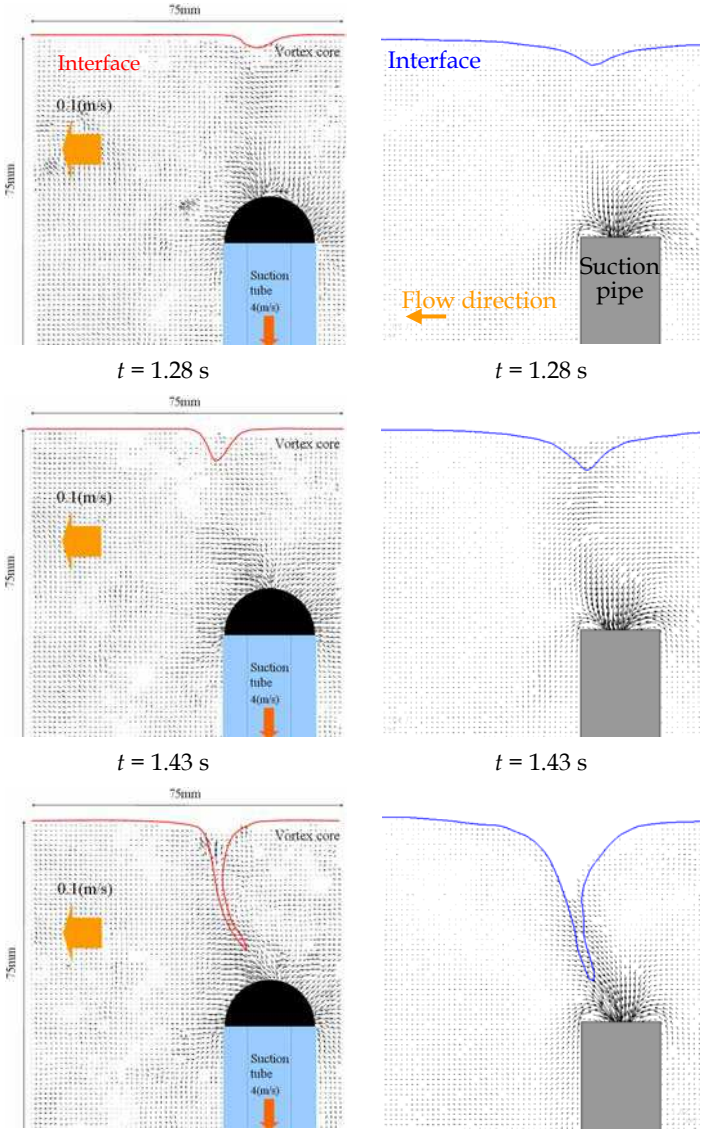

Fig. 18. Comparison of gas core elongation behavior in experimental and simulation results

simulation result shows clearly that the gas core is elongated along the region with the high downward velocity when the downward velocity develops toward the gas-liquid interface. This tendency is observed also in the experimental result and is reported by Okamoto (Okamoto et al., 2004) as the occurrence mechanism of the GE phenomena in the simple experiment. Therefore, it is confirmed that the GE phenomena in the simulation result is induced by the same mechanism as that in the experiment. From these simulation results, the developed high-precision numerical simulation algorithms are validated to be capable of reproducing the GE phenomena.

5. Conclusion

As an example of the evaluation of interfacial flows, two methodologies were proposed for the evaluation of the GE phenomena. One is the CFD-based prediction methodology and the other is the high-precision numerical simulation of interfacial flows.

In the development of the CFD-based prediction methodology, the vortical flow model was firstly constructed based on the Burgers theory. Then, the accuracy of the CFD results, which are obtained on relatively coarse computational mesh without considering interfacial deformations for the reduction of the computational costs, was discussed to determine the occurrence indicators of the two types of the GE phenomena, i.e. the elongated gas core type and the bubble pinch-off type. In this study, the gas core length was selected as the indicator of the elongated gas core type with considering the three times allowance. On the other hand, the downward velocity gradient was determined empirically as the indicator of the bubble pinch-off type. Finally, the developed CFD-based prediction methodology was applied to the evaluation of the GE phenomena in an experiment using 1/1.8 scale partial model of the upper plenum in reactor vessel of a large-scale FR. As a result, the GE occurrence observed in the 1/1.8 scale partial model experiment was evaluated correctly by the CFD-based prediction methodology. Therefore, it was confirmed that the CFD-based prediction methodology can evaluate the GE phenomena properly with relatively low computational costs.

In the development of the high-precision numerical simulation algorithms, the high-precision volume-of-fluid algorithm, i.e. the PLIC algorithm, was employed as the interface-tracking algorithm. Then, to satisfy the requirement for accurate geometrical modeling of complicated spatial configurations, an unstructured mesh scheme was employed, so that the PLIC algorithm was newly developed on unstructured meshes. Namely, the algorithms for the calculation of the unit vector normal to an interface, reconstruction of an interface, volume fraction transport through cell-faces and surface tension were newly developed for high accurate simulations on unstructured meshes. In addition, to establish the volume conservation property violated by the excess or too little transport of the volume fraction, the volume conservative algorithm was developed by introducing the physics-basis correction algorithm. Physics-basis considerations were also conducted for mechanical balances at gas-liquid interfaces. By defining momentum and velocity independently at gas-liquid interfaces, the physically appropriate formulation of momentum transport was derived, which can eliminate unphysical behaviors near the gas-liquid interfaces caused by conventional formulations. Furthermore, the improvement was necessary to satisfy the mechanically appropriate balances between pressure and surface tension at gas-liquid interfaces, so that the physically appropriate formulation was also derived for the pressure gradient calculation at gas-liquid interfaces. As the verification of the developed PLIC

algorithm, the slotted-disk revolution problem was solved on the unstructured mesh, and the simulation result showed that the accurate interface-tracking could be achieved even on unstructured meshes. The volume conservation algorithm was also confirmed to be efficient to enhance highly the simulation accuracy on unstructured meshes. Finally, the GE phenomena in the simple experiment were simulated. For the numerical simulation, the unstructured mesh was carefully considered to determine the size of cells in the central region of the vortical flow. In the simulation result, the GE phenomena observed in the experiment was reproduced successfully. In particular, the shape of the elongated gas core was very similar with the experimental result. Therefore, it was validated that the high-precision numerical simulation algorithms developed in this study could simulate accurately the transient behaviors of the GE phenomena.

6. References

Andersen, A.; Bohr, T.; Stenum, B.; Juul Rasmussen, J. & Lautrup, B. (2003). Anatomy of a bathtub vortex, *Physical Review Letters*, Vol. 91, No. 10, 104502-1-104502-4.

Brackbill, J. U. D.; Kothe, B. & Zemach, C. (1992). A continuum method for modeling surface tension, *J. Comput. Phys.*, Vol. 100, Issue. 2, 335-354.

Burgers, J. M. (1948). A mathematical model illustrating the theory of turbulence, In: *Advance in applied mechanics,* Mises, R. & Karman, T., Eds., 171-199, Academic Press, New York.

Craya, A. (1949). Theoretical research on the flow of nonhomogeneous fluids, *La Houille Blanche,* Vol. 4, 22-55.

Cummins, S. J.; Francois M. M. & Kothe, D. B. (2005). Estimating curvature from volume fractions, *Computer & Structure,* Vol. 83, 425-434.

Daggett, L. L. & Keulegan, G. H. (1974). Similitude in free-surface vortex formations, *Journal of the Hydraulics Division, Proceedings of the ASCE,* Vol. 100, HY8.

Eguchi, Y.; Yamamoto, K.; Funada, T.; Tanaka, N.; Moriya, S.; Tanimoto, K.; Ogura, K.; Suzuki, K. & Maekawa, I. (1984). Gas entrainment in the IHX of top-entry loop-type LMFBR, *Nuclear Engineering and Design,* Vol. 146, 373-381.

Harvie, D. J. E. & Fletcher, D. F. (2000). A new volume of fluid advection algorithm: the Stream scheme, *Journal of Computational Physics,* Vol. 162, 1-32.

Hirt, C. W. & Nichols, D. B. (1981). Volume of fluid (VOF) method for the dynamics of free boundaries, *Journal of Computational Physics,* Vol. 39, 201-205.

Hunt, J.; Wray, A. & Moin, P. (1988). Eddies, stream and convergence zones in turbulent flows, *Center for Turbulence Research report*, CTR-S88.

Ito, K.; Yamamoto, Y. & Kunugi, T. (2007). Development of numerical method for simulation of gas entrainment phenomena, *Proceedings of the Twelfth International Topical Meeting on Nuclear Reactor Thermal Hydraulics*, No. 121, Sheraton station square, September 2007, Pittsburgh, PA.

Ito, K.; Eguchi, Y.; Monji, H.; Ohshima, H.; Uchibori, A. & Xu, Y. (2008). Improvement of gas entrainment evaluation method –introduction of surface tension effect–, *Proceedings of Sixth Japan-Korea Symposium on Nuclear Thermal Hydraulics and Safety*, No. N6P1052, Bankoku-shinryokan, November 2008, Okinawa, Japan.

Ito, K.; Kunugi, T.; Ohshima, H. & Kawamura, T. (2009) Formulations and validations of a high-precision volume-of-fluid algorithm on non-orthogonal meshes for numerical

simulations of gas entrainment phenomena, *Journal of Nuclear Science and Technology,* Vol. 46, 366-373.

Ito. K & Kunugi, T. Appropriate formulations for velocity and pressure calculations at gas-liquid interface with collocated variable arrangement, *Journal of Fluid Science and Technology* (submitted).

Kim, S. E.; Makarov, B. & Caraeni, D. (2003) A multi-dimensional linear reconstruction scheme for arbitrary unstructured grids, *Proceedings of 16th AIAA Computational Fluid Dynamics Conference*, pp. 1436-1446, June 2003, Orlando, FL.

Kimura, N.; Ezure, T.; Tobita, A. & Kamide, H. (2008). Experimental study on gas entrainment at free surface in reactor vessel of a compact sodium-cooled fast reactor, *Journal of Nuclear Science and Technology,* Vol. 45, 1053-1062.

Kunugi, T. (2001). MARS for multiphase calculation, *Computational Fluid Dynamics Journal,* Vol. 19, 563-571.

Maier, M. R. (1998). Onsets of liquid and gas entrainment during discharge from a stratified air-water region through two horizontal side branches with centerlines falling in an inclined plane, *Master of Science Thesis*, University of Manitoba.

Monji, H.; Akimoto, T.; Miwa, D. & Kamide, H. (2004). Unsteady behavior of gas entraining vortex on free surface in cylindrical vessel, *Proceedings of Fourth Japan-Korea Symposium on Nuclear Thermal Hydraulics and Safety*, pp. 190-194, Hokkaido University, November 2004, Sapporo, Japan.

Moriya, S. (1998). Estimation of hydraulic characteristics of free surface vortices on the basis of extension vortex theory and fine model test measurements, *CRIEPI Abiko Research Laboratory Report,* No. U97072 (in Japanese).

Nagata, T. (2008). Early commercialization of fast reactor cycle in Japan, *Proceedings of the 16th Pacific Basin Nuclear Conference*, October 2008, Aomori, Japan.

Noh, W. F. & Woodward, P. (1976). SLIC (simple line interface calculation), *Lecture Notes in Physics,* van der Vooren, A. I. & Zandbergen, P. J., Eds., 330-340, Springer-Verlag.

Okamoto, K.; Takeyama, K. & Iida, M. (2004). Dynamic PIV measurement for the transient behavior of a free-surface vortex, *Proceedings of Fourth Japan-Korea Symposium on Nuclear Thermal Hydraulics and Safety*, pp. 186-189, Hokkaido University, November 2004, Sapporo, Japan.

Pilliod, J. E. & Puckett, E. G. (2004). Second-order accurate volume-of-fluid algorithms for tracking material interfaces, *Journal of Computational Physics,* Vol. 199, 465-502.

Renardy, Y. & Renardy, M. (2002). PROST: A parabolic reconstruction of surface tension for the volume-of-fluid method, *Journal of Computational Physics,* Vol. 183, 400–421.

Rider, W. & Kothe, D. B. (1998). Reconstructing volume tracking, *Journal of Computational Physics,* Vol. 141, 112-152.

Rudman, M. (1997). Volume-tracking methods for interfacial flow calculations, *International Journal for Numerical Methods in Fluids,* Vol. 24, 671-691.

Sakai, S.; Madarame, H. & Okamoto, K. (1997). Measurement of flow distribution around a bathtub vortex, *Transaction of the Japan Society of Mechanical Engineers, Series B*, Vol. 63, No. 614, 3223-3230 (in Japanese).

Sakai, T.; Eguchi, Y.; Monji, H.; Ito, K. & Ohshima, H. (2008). Proposal of design criteria for gas entrainment from vortex dimples based on a computational fluid dynamics method, *Heat Transfer Engineering,* Vol. 29, 731-739.

Scardvelli, R. & Zaleski, S. (2000). Analytical relations connecting linear interface and volume functions in rectangular grids, *Journal of Computational Physics,* Vol. 164, 228-237.

Ubbink, O. & Issa, R. I. (1999). A method for capturing sharp fluid interfaces on arbitrary meshes, *Journal of Computational Physics,* Vol. 153, 26-50.

Uchibori, A.; Sakai, T. & Ohshima, H. (2006). Numerical prediction of gas entrainment in the 1/1.8 scaled partial model of the upper plenum, *Proceedings of Fifth Japan-Korea Symposium on Nuclear Thermal Hydraulics and Safety*, pp. 414-420, Ramada Plaza Hotel, November 2006, Jeju, Korea.

Yang, X. & James, A. J. (2006). Analytic relations for reconstructing piecewise linear interfaces in triangular and tetrahedral grids, *Journal of Computational Physics,* Vol. 214, 41-54.

Youngs, D. L. (1982). Time-dependent multi-material flow with large fluid distortion, *Numerical Methods for Fluid Dynamics,* Morton, K. W. & Baines, M. J. Eds., 273-486, American Press, New York.

Zalesak, S. T. (1979). Fully multidimensional flux-corrected transport algorithm for fluids, *Journal of Computational Physics,* Vol. 31, 335-362.

Zuber, N. (1980). Problems in modeling of small break LOCA, *Nuclear Regulatory Commission Report,* NUREG-0724.

Computational Fluid Dynamics

Edited by Hyoung Woo Oh

ISBN 978-953-7619-59-6
Hard cover, 420 pages
Publisher InTech
Published online 01, January, 2010
Published in print edition January, 2010

This book is intended to serve as a reference text for advanced scientists and research engineers to solve a variety of fluid flow problems using computational fluid dynamics (CFD). Each chapter arises from a collection of research papers and discussions contributed by the practiced experts in the field of fluid mechanics. This material has encompassed a wide range of CFD applications concerning computational scheme, turbulence modeling and its simulation, multiphase flow modeling, unsteady-flow computation, and industrial applications of CFD.

InTech Europe
University Campus STeP Ri
Slavka Krautzeka 83/A
51000 Rijeka, Croatia
Phone: +385 (51) 770 447
Fax: +385 (51) 686 166
www.intechopen.com

InTech China
Unit 405, Office Block, Hotel Equatorial Shanghai
No.65, Yan An Road (West), Shanghai, 200040, China
中国上海市延安西路65号上海国际贵都大饭店办公楼405单元
Phone: +86-21-62489820
Fax: +86-21-62489821